Site selection of desert solar farms based on heterogeneous sand flux

Guoshuai Li[1, 2], Lihai Tan[3], Bao Yang[4], Tao Che[1], Guangcai Feng[5], Fredrik Charpentier Ljungqvist[6, 7, 8], Yayong Luo[9], Heqiang Du[10], Hui Zhao[10], Ying Zhang[1], Chunlin Huang[1], Ning Huang[11], Wenjun Tang[2], Rui Jin[1], and Xin Li[2]

[1]Heihe Remote Sensing Experimental Research Station, Northwest Institute of Eco-Environment and Resources, Chinese Academy of Sciences, Lanzhou, China
[2]National Tibetan Plateau Data Center, State Key Laboratory of Tibetan Plateau Earth System, Environment and Resources, Institute of Tibetan Plateau Research, Chinese Academy of Sciences, Beijing, China
[3]Dunhuang Gobi Desert Research Station, Northwest Institute of Eco-Environment and Resources, Chinese Academy of Sciences, Lanzhou, China
[4]School of Geography and Ocean Science, Nanjing University, Nanjing, China
[5]School of Geosciences and Info-physics, Central South University, Changsha, China
[6]Department of History, Stockholm University, Stockholm, Sweden
[7]Bolin Centre for Climate Research, Stockholm University, Stockholm, Sweden
[8]Swedish Collegium for Advanced Study, Uppsala, Sweden
[9]Naiman Desertification Research Station, Northwest Institute of Eco-Environment and Resources, Chinese Academy of Sciences, Lanzhou, China
[10]Key Laboratory of Desert and Desertification, Northwest Institute of Eco-Environment and Resources, Chinese Academy of Sciences, Lanzhou, China
[11]Department of Mechanics, College of Civil Engineering and Mechanics, Lanzhou University, Lanzhou, China

Correspondence to: Xin Li, xinli@itpcas.ac.cn

Abstract

Site selection for building solar farms in deserts is crucial and must consider the dune threats associated with sand flux, such as sand burial and dust contamination. Understanding the changes in sand flux can optimize the site selection of desert solar farms. Here we use the ERA5-Land hourly wind data with 0.1°×0.1° resolution to calculate the yearly sand flux from 1950 to 2022. The mean of sand flux is used to score the suitability of global deserts for building solar farms. We find that the majority of global deserts have low flux potential (≤40 m^3 m^{-1} yr^{-1}) and resultant flux potential (≤2.0 m^3 m^{-1} yr^{-1}) over the past 73 years. The scoring result demonstrates presents that global deserts have obvious patch distribution of site suitability for building solar farms. Our study optimizes the site selection of desert solar farms, which aligns with the United Nations sustainability development goals for achieving affordable and clean energy target by 2030.

INTRODUCTION

Increasing the share of renewable energy is essential to realize the global emission reduction targets[1, 2]. According to the current global emission reduction trends, it is difficult to achieve the global 1.5°C/2°C temperature increase goals and 2050/2070 net-zero emission targets[3–5]. To reduce anthropogenic carbon dioxide emissions, the exploration of renewable energy at a global scale need be strengthened[1, 6, 7]. In recent years, solar energy, as affordable and clean energy, has been increasingly utilized[8]. A large number of solar farms have been built across the globe[8, 9]. Deserts with low land value and long sunshine time are favorable for building solar farms[10, 11]. In turn, solar farms in deserts can increase surface friction, reduce surface albedo, enhance local precipitation, and flourish regional vegetation around deserts[10]. Hence, desert solar geoengineering should be considered a feasible action program of planetary geoengineering[12, 13] aiming at mitigating anthropogenic greenhouse gas emissions. For building desert solar farms, the existing site suitability methodologies[14–16] can not effectively solve the dune threats (e.g. sand burial and dust contamination) to solar photovoltaic panels across global deserts.

Dune threats are associated with sand flux, and sand flux driven by effective shear velocities reflects the potential sediment transport capacity of the wind[17–24]. Sand flux in this study can be briefly quantified through the flux potential (FP) and resultant flux potential (RFP). This is similar to the drift potential and resultant drift potential of sand drift[25–27], the absolute potential sand flux and resultant potential sand flux[18–20]. FP is the sum of bulk fluxes in all azimuths, and RFP is calculated by the Euclidean formula of the projected due-north and due-east bulk flux components from all azimuths[28] (METHODS). Note that the flux calculation is for the saturated flux. The true flux may be smaller (due to precipitation or erodible surface fraction) or larger (due to dune steepness), but this is a reasonable estimate with precedents in other studies[18–21]. FP and RFP of sand flux have been used to quantify dune activities[18–21]. Theoretically, FP represents wind energy, so higher FP means greater transport capacity of instantaneous winds in all azimuths; RFP represents the net sand transport potential in the resultant flux direction, so higher RFP means severer accumulation[25,26]; FP is more important than RFP in assessing the dune threats. Most studies of sand flux are based on the wind data from local meteorological stations[29]. However, global meteorological stations are limited in deserts[27]. Wind data from the reanalysis products with different spatiotemporal resolutions provide a feasible scheme for quantifying sand flux at a global scale[18–21]. For example, the ERA5 reanalysis product (0.25°×0.25° resolution)[30] was used to calculate the FP and RFP of sand flux[18–20]. Accordingly, the one-hour-scale instantaneous wind data from the ERA5-Land reanalysis product with high resolution (0.1°×0.1°)[31] should be able to adequately capture more spatial details of sand flux changes[21], and then assess the dune threats to desert solar farms. However, how to use the FP and RFP to effectively optimize the site selection of solar farms across global deserts remains unsolved.

In this study, we resample desertified lands and sandy lands at 500 m resolution (extracted by the support vector machine analysis, trial-and-error method and visual interpretation analyses based on the Moderate resolution Imaging Spectroradiometer data)[32] into global deserts at 0.1°×0.1° resolution (Fig. 1). We use the eastward and northward wind components at the height of 10 m from the ERA5-Land hourly wind data to calculate the yearly sand flux for the period 1950–2022, and adopt the 73-yr mean sand flux to assess the suitability of global deserts for building solar farms. According to solar farm scores, we can reduce or avoid the dune threats, and efficiently operate desert solar farms.

Results

73-yr mean sand flux

Global deserts with 0.1°×0.1° resolution were distributed in 55 countries, including 23 countries in Asia, 20 countries in Africa, 4 countries in South America, 2 countries in North America, 1 country in Europe and 1 country in Australasia (Fig. 1).

We calculated the yearly FP and RFP from the ERA5-Land hourly wind data (METHODS). During 1950–2022, the FP mean of global deserts was 23.7±3.9 m^3 m^{-1} yr^{-1} (mean ± standard deviation), with the maximum mean and standard deviation of 282.1 m^3 m^{-1} yr^{-1} and 26.5 m^3 m^{-1} yr^{-1} on the ERA5-Land grid-scale, respectively. The FP means had patchy distribution globally. In terms of the ERA5-Land grid point number, the FP means of 0–20 m^3 m^{-1} yr^{-1} were dominant, and followed by the patches of 20–40 m^3 m^{-1} yr^{-1}. The FP means greater than 40 m^3 m^{-1} yr^{-1} are shown in Fig. 2a.

The RFP mean of global deserts was 0.7±0.4 m^3 m^{-1} yr^{-1}, with the maximum mean and standard deviation of 11.8 m^3 m^{-1} yr^{-1} and 4.1 m^3 m^{-1} yr^{-1} on the grid-scale, respectively. The RFP means also had patchy distribution across global deserts. Most deserts were dominated by the patches with the RFP means of 0–1.0 m^3 m^{-1} yr^{-1}, and then the patches of 1.0–2.0 m^3 m^{-1} yr^{-1}. The patches with the RFP mean greater than

2.0 m^3 m^{-1} yr^{-1} are shown in Fig. 2b. The patches with high RFP mean may have high dune celerities[28, 33]. The spatial distributions of the FP and RFP standard deviations can be seen in Fig. S1.

In this study, the spatial distributions of the 73-yr mean FP and RFP calculated by the one-hour-scale instantaneous wind data from the ERA5-Land reanalysis product were similar to those of the 15-yr mean drift potential and resultant drift potential calculated by the fifteen-minute-scale instantaneous wind simulations from the HadGEM3-GC3.1 model family for the period 2000–2015[27]. This suggests that the interpolation from ERA5 to ERA5-Land hourly wind data[31] does not filter out high wind speed events[27], and the ERA5-Land hourly wind data effectively capture the basic characteristics of sand flux across global deserts.

Scoring scheme for desert solar farms

We classified the 73-yr mean sand flux to construct a scoring scheme. First, the FP and RFP means were used to quantify the sand burial degree, and the FP means were used to distinguish the dust contamination degree. Then, we divided the FP means and the RFP means into 4 classes separately using quartile classification (Fig. 3a and Fig. 3b), intersected the FP mean classes and the RFP mean classes, removed the non-observed permutations and scored the suitability according to the applied rule, in which we assumed that the FP mean is more important than the RFP mean in scoring the suitability of global deserts due to low solar photovoltaic panels (METHODS).

The first step of the scoring scheme is to divide the FP means into 4 classes using the FP mean quartiles: the first quartile (13.2 m^3 m^{-1} yr^{-1}), the median (21.2 m^3 m^{-1} yr^{-1}) and the third quartile (30.1 m^3 m^{-1} yr^{-1}). These classes had the geodesic area of 2706.9×10^3 km^2, 2720.4×10^3 km^2, 2665.0×10^3 km^2 and 2638.8×10^3 km^2, respectively (Fig. 3a). The second step is to divide the RFP means into 4 classes using the RFP mean quartiles: the first quartile (0.5 m^3 m^{-1} yr^{-1}), the median (0.6 m^3 m^{-1} yr^{-1}) and the third quartile (0.8 m^3 m^{-1} yr^{-1}). These classes had the geodesic area of 2736.8×10^3 km^2, 2730.0×10^3 km^2, 2649.9×10^3 km^2 and 2614.2×10^3 km^2, respectively (Fig. 3b). The final step is to intersect the FP and RFP mean classes. We removed the non-observed permutations and got the scores of solar farms according to the applied rule. The ascending FP and RFP mean classes are unfavorable for solar farms (Table 1, more details see METHODS).

Solar farm scores based on quartile classification of the FP and RFP means showed obvious patch distribution across global deserts. For solar farms, the highest score 15 had the maximum grid point number of 21068 and geodesic area of 2333.3×10^3 km^2. In contrast, score 12 had the minimum grid point number of 1 and geodesic area of 0.1×10^3 km^2. For the rest, see Fig. 3c inset and Table 1. If only consider the dune threats, high (low) scores clearly showed that global deserts had strong (weak) suitability for building solar farms. In conclusion, the criteria of site selection for solar farms varied across the globe.

DISCUSSION

Our results demonstrate heterogeneous spatial distribution of sand flux and wind environment classifications of global deserts, and present a scoring scheme for the site selection of solar farms across global deserts on the basis of the 73-yr mean sand flux that reflects the basic characteristics of sand flux. In this study, we assumed that the FP mean is more important than the RFP mean in evaluating the threats to low solar photovoltaic panels. The FP is intercepted by solar photovoltaic panels because a solar farm represents a local sink area. High FP brings severe sandblasting[34, 35] and causes severe dust contamination on solar photovoltaic panels. The RFP causes the sand burial of solar photovoltaic panels in the resultant flux direction. In addition, we adopt the quartile classification of the FP and RFP mean distributions to ensure the logical rationality of the scoring scheme. Furthermore, we find 47.2% of the existing solar installation sites[36] in deserts are located in the highest-score regions of solar farms (Fig. 4 and Table 1). The inconsistency of score orders sorted by area percentage and scoring frequency also reflect the robustness of our scoring scheme (Fig. 3, Fig. 4 and Table 1).

This study provides a guide to select the regions suitable for desert solar farms. Using the wind data from the reanalysis products with different spatiotemporal resolutions[18–21], especially, the ERA5-Land reanalysis product (0.1°×0.1° and hourly resolution)[21], could detailedly characterize the wind environments and quantify the dune threats at a global scale. In this study, we neglect the errors introduced by the interpolation from the ERA5 to ERA5-Land hourly wind data, especially in complex terrains or coastal areas[31]. Some deserts have no effective shear velocities and small or zero flux[18–20, 26]. They may be interpreted as the ancient dune systems or be driven by other episodic factors (e.g. alluvial/fluvial, lacustrine and coastal). But this study only focuses on the potential sediment transport capacity determined by effective shear velocities[17–24]. In the actual site selection, local situations such as sediment availability[37], topographic influences[38, 39] and precipitation effect[19, 40] should also be considered.

Our scoring scheme could be used to choose the best sites for solar farms in the regions affected by dune threats, and to assess the site selection of traffic engineering, petroleum exploitation and irrigated farming in desert environments. Our results can help improve desert solar geoengineering and achieve the Sustainable Development Goal 7 ("affordable, reliable, sustainable and modern energy for all") by 2030[41], and may even contributes to maintaining the global surface temperature anomaly of 1.5–2°C and reaching the global carbon neutrality[42] over the long-term.

METHODS

Desert data

Wu et al., 2022[32] extracted the Moderate Resolution Imaging Spectroradiometer

(MODIS) Terra MOD09A1 product with 500 m resolution from the bare ground areas during 2015[43]. Next, they used the independent components analysis tool to enhance the spectra of the mosaiced MOD09A1 product. After that the support vector machine method trained on 80612 samples was employed to extract the desert areas, achieving a classification accuracy of 79.83% for 50226 test samples. Then, they used the trial-and-error method to extract the areas with the relief degree ≤ 500 m. This improved the classification accuracy to 81.87%. Later, they used the Google Earth's high-resolution satellite image to visually interpret and identify the areas that cannot be distinguished by machine learning. By doing this, the classification accuracy of desert areas reached to 92.37%. Finally, land cover types in desert areas included grassland, shrub, desertified land and sandy land, and gobi covers[32]. In this study, we referred to desertified lands and sandy lands as global deserts, and assumed that global deserts are covered by medium-to-fine sands.

We used the 73-yr mean FP as the snap raster to resample desertified lands and sandy lands with 500 m resolution into global deserts at 0.1°×0.1° resolution, the same to the spatial resolution of the ERA5-Land reanalysis product from the European Center for Medium Range Weather Forecasts (ECMWF)[31]. The grid point number and geodesic area of global deserts were 98380 and 10731.0×10^3 km^2, respectively.

Wind data

Wind data are from the eastward and northward wind components at the height of 10 m of the ERA5-Land reanalysis product, which has the hourly temporal resolution and 0.1°×0.1° spatial resolution[31]. In this study, the ERA5-Land hourly wind data spanned from 1950 to 2022. The instantaneous wind speed U and azimuth A at the height of 10 m is calculated as

$$U = \sqrt[2]{u^2 + v^2} \tag{1}$$

$$A = atan2(u, v) \tag{2}$$

where u is the eastward component, in m s^{-1}; and v is the northward component, in m s^{-1}. Note that the ERA5-Land eastward and northward wind components are got by simply linear interpolating the ERA5 eastward and northward wind components based on a triangular mesh. They are not model output of the ECMWF land surface model at 0.1°×0.1° resolution[31].

Conceptual framework of sand flux

The shear velocity u_* in m s^{-1} is calculated as

$$u_* = \frac{U\kappa}{ln(z/z_0)} \tag{3}$$

where U is the instantaneous wind speed at the height of 10 m, κ = 0.4 is Von Kármán constant, z = 10 m is the height above the Earth surface, z_0 = 0.001 m is the assumed roughness length above the sand surface[44].

The impact threshold shear velocity u_{*t} = 0.231 m s^{-1} is calculated by

$$u_{*t} = \frac{\sqrt[2]{g d \rho_s/\rho_f}}{10} \tag{4}$$

where g = 9.81 m^2 s^{-1} is gravity acceleration; d = 0.00025 m is the reference median grain diameter of medium-to-fine sands for active deserts[45–47]; ρ_s = 2650 kg m^{-3} is sand density; ρ_f = 1.22 kg m^{-3} is air density[23, 45].

The saturated bulk flux $\overrightarrow{q_b}$ in m^3 m^{-1} s^{-1} is approximately[22–24]

$$\overrightarrow{q_b} = C \frac{u_{*t}}{g \rho_b} \rho_f (u_{*e}^2 - u_{*t}^2) \tag{5}$$

where C = 5 is an empirical (dimensionless) scaling parameter, ρ_b = 1580 kg m^{-3} is the mean of bulk densities in other studies[48–59] (Table S1), $u_{*e} = u_* > u_{*t}$ is the effective shear velocity.

After deriving the effective shear velocity, and considering the intermittence of instantaneous winds, we also define $\overrightarrow{q_b} = 0$ when $u_* \leq u_{*t}$, and finally apply zero flux to the mean of the subsequent flux calculations, so the mean hourly flux vector lengths Q_b in m^3 m^{-1} s^{-1} and the mean hourly flux vectors Q_r in m^3 m^{-1} s^{-1}[27–29] are given by

$$Q_b = \frac{\sum_{i=1}^{N} |\overrightarrow{q_b}|}{N} \tag{6}$$

$$Q_r = \sqrt[2]{\left(\frac{\sum_{i=1}^{N} \overrightarrow{q_b} \sin A}{N}\right)^2 + \left(\frac{\sum_{i=1}^{N} \overrightarrow{q_b} \cos A}{N}\right)^2} \tag{7}$$

where N is the number of hours in a Julian year (8760 hours for a common year and 8784 hours for a leap year), and it represents the 8760 or 8784 instantaneous wind vector measurements[19] with the one-hour sampling rate[28]. We only focus on the ERA5-Land hourly wind data in this study. This means we do not consider the influence from different temporal resolutions or different averaging time intervals of other wind data[27, 29]. However, the one-hour-scale instantaneous wind data may underestimate the true bulk flux, because it cannot capture high wind speed events as effectively as the ten-minute-scale standard meteorological data[27, 29].

Finally, the flux potential (FP) and resultant flux potential (RFP) measured in m^3 m^{-1} yr^{-1} are defined as

$$\text{FP} = S Q_b \tag{8}$$

$$\mathrm{RFP} = SQ_r \tag{9}$$

where S = 31536000 is the conversion factor from second to year (365 days). The FP (a scalar value) is the sum of bulk fluxes in all azimuths, and it represents the transport capacity of instantaneous winds in all azimuths. The RFP (a net resultant vector) is the Euclidean sum of the projected due-east and due-north bulk flux components from all azimuths, and it represents the net sand transport potential in the resultant flux direction, which is the net trend of sand flux, in line with the dominant direction of dune celerities[28, 33]. We used the absolute RFP, neglecting its vector property.

In addition, the naming directions of FP and RFP follows where the sand moves. Eventually, the ERA5-Land grid cells in deserts pile up sand measured by RFP under effective shear velocities.

Calculating the 73-yr mean sand flux

We estimated the spatial distributions of the FP and RFP means across global dunes. Considering the uncertainty of wind speed from the ERA5-Land hourly wind data[31], we extracted the spatial distributions of the standard deviations of the FP and RFP means during the study period (Fig. S1).

Area-weighted aggregated statistics

The means ± standard deviations of FP and RFP for global deserts were weighted by the grid cell area at a global scale, employing the CDO software[60].

Rule of the scoring scheme

For interpretation and application, we divided the FP mean and the RFP mean into 4 classes separately using quartiles. The quartiles of the FP means were 13.2 m^3 m^{-1} yr^{-1} (the first quartile), 21.2 m^3 m^{-1} yr^{-1} (the median) and 30.1 m^3 m^{-1} yr^{-1} (the third quartile). For the RFP means, the quartiles were 0.5 m^3 m^{-1} yr^{-1} (the first quartile), 0.6 m^3 m^{-1} yr^{-1} (the median) and 0.8 m^3 m^{-1} yr^{-1} (the third quartile). For solar farms, FP reflects both the potential sand burial degree in all azimuths and the dust contamination degree on solar photovoltaic panels. High FP brings sandblasting[34, 35], and produces dusts that cover solar photovoltaic panel surface, reducing the solar photovoltaic conversion efficiency[61]. RFP reflects the potential sand burial degree of low solar photovoltaic panels in the resultant flux direction.

In our scoring scheme, due to low solar photovoltaic panels, we assigned greater importance to the FP mean over the RFP mean when scoring the suitability of global deserts. Higher FP and RFP means indicate less favorable conditions for solar farms. On the basis of the above empirical judgement, we applied one simple rule for scoring the suitability of geometric intersections between the FP and RFP mean classes.

We tabulated the solar farm score by the importance of empirical judgment about solar farms. The permutation number of the FP and RFP mean classes in sand flux was 16 (4×4).

The scoring scheme for solar farms included the following steps:

Step 1: Sort the FP mean class in the first column from high to low.

Step 2: In the second column, we still sequentially nested the RFP mean class from high to low under individual classes of the FP mean (from high to low).

Step 3: Considering the empirical judgment about solar farms, we assigned the score from 1 to 16. However, only one permutation was not observed at a global scale. We removed this permutation and reassigned the final solar farm score from 1 to 15 (Table 1).

Validation of the scoring scheme

The locations of solar installations used for the validation are from the global, open-access, harmonized spatial datasets based on the OpenStreetMap infrastructure data[36,62]. We used the desert data to mask the point vector data titled by the global_solar_2020, and identified the actual locations of solar installations in deserts (Fig. 4 and Table 1), in order to validate the robustness of our scoring scheme for solar farms in deserts.

DATA AVAILABILITY

The dataset generated in this study are publicly available via the National Tibetan Plateau Data Center (https://doi.org/10.11888/Terre.tpdc.300853).

CODE AVAILABILITY

Codes for calculating the yearly sand flux based on the ERA5-Land hourly wind data are available at https://github.com/liguoshuai-desert/wind-flux. Data analysis is finished by the CDO, Python, ArcGIS 10.6 and OriginPro Learning Edition software.

References

1 Arent, D. J., Wise, A. & Gelman, R. The status and prospects of renewable energy for combating global warming. *Energ. Econ.* **33**, 584-593 (2011).

2 Yang, Q. et al. Prospective contributions of biomass pyrolysis to China's 2050 carbon reduction and renewable energy goals. *Nat. Commun.* **12**, 1698 (2021).

3 United Naitons Environment Programme. *Emissions Gap Report 2021: The Heat Is On – A World of Climate Promises Not Yet Delivered*. Nairobi (2021).

4 Arias, P. A. et al. *Technical Summary*. in *Climate Change 2021: The Physical Science Basis. Contribution of Working Group I to the Sixth Assessment Report of the Intergovernmental Panel on Climate Change* [Masson-Delmotte V., P. Zhai, A. Pirani, S. L. Connors, C. Péan, S. Berger, N. Caud, Y. Chen, L. Goldfarb, M. I. Gomis, M. Huang, K. Leitzell, E. Lonnoy, J.B.R. Matthews, T. K. Maycock, T. Waterfield, O. Yelekçi, R. Yu and B. Zhou (eds.)]. Cambridge University Press, In Press (2021).

5 IPCC. *Summary for Policymakers*. In *Global Warming of 1.5°C. An IPCC Special Report on the impacts of global warming of 1.5°C above pre-industrial levels and related global greenhouse gas emission pathways, in the context of strengthening the global response to the threat of climate change, sustainable development, and efforts to eradicate poverty*. [Masson-Delmotte, V., P. Zhai, H.-O. Pörtner, D. Roberts, J. Skea, P.R. Shukla, A. Pirani, W. Moufouma-Okia, C. Péan, R. Pidcock, S. Connors, J.B.R. Matthews, Y. Chen, X. Zhou, M.I. Gomis, E. Lonnoy, T. Maycock, M. Tignor, and T. Waterfield (eds.)]. In Press (2018).

6 Fornasiero, P. & Graziani, M. *Renewable resources and renewable energy: a global challenge*. CRC press (2011).

7 Hao, F. & Shao, W. What really drives the deployment of renewable energy? A global assessment of 118 countries. *Energy Res. Soc. Sci.* **72**, 101880 (2021).

8 Kruitwagen, L. et al. A global inventory of photovoltaic solar energy generating units. *Nature* **598**, 604–610 (2021).

9 Dowers, B. *Wind farms and solar PV panels in the landscape*. In *Reference Module in Earth Systems and Environmental Sciences*. Elsevier (2020).

10 Li, Y. et al. Climate model shows large-scale wind and solar farms in the Sahara increase rain and vegetation. *Science* **361**, 1019-1022 (2018).

11 Lu, Z. et al. Impacts of large-scale Sahara solar farms on global climate and vegetation cover. *Geophys. Res. Lett.* **48**, e2020GL090789 (2021).

12 Moore, J. C., Jevrejeva, S. & Grinsted, A. Efficacy of geoengineering to limit 21st century sea-level rise. *Proc. Natl. Acad. Sci. USA* **107**, 15699-15703 (2010).

13 Matthews, H. D. & Caldeira, K. Transient climate–carbon simulations of planetary geoengineering. *Proc. Natl. Acad. Sci. USA* **104**, 9949-9954 (2007).

14. Al Garni, H. Z. & Awasthi, A. *Solar PV power plants site selection: a review*. In *Advances in Renewable Energies and Power Technologies*, [Yahyaoui, I. (ed.)]. Elsevier, 57-75 (2018).

15. Al-Dousari, A. et al. Solar and wind energy: Challenges and solutions in desert regions. *Energy* 176, 184-194 (2019).

16. Ehara, T., Komoto, K. & van der Vleuten, P. *Very large photovoltaic systems in deserts*. in *Reference Module in Earth Systems and Environmental Sciences. Elsevier* (2021).

17 Kocurek, G. *The aeolian rock record (Yes, Virginia, it exists, but it really is*

rather special to create one). In *Aeolian Environments, Sediments and Landforms* [Andrew S. Goudie, Ian Livingstone, & Stephen Stokes (eds.)]. John Wiley and Sons Ltd, 239-259 (1999).

18 Gunn, A. et al., What sets aeolian dune height? *Nat. Commun.* **13**, 2401 (2022).

19 Gunn, A., East, A. & Jerolmack, D. J. 21st-century stagnation in unvegetated sand-sea activity. *Nat. Commun.* **13**, 3670 (2022).

20 Gunn, A. et al., Circadian rhythm of dune-field activity. *Geophys. Res. Lett.* **48**, e2020GL090924 (2021).

21 Chanteloube, C. et al., Source-to-sink aeolian fluxes from arid landscape dynamics in the Lut Desert. *Geophys. Res. Lett.* **49**, e2021GL097342 (2022).

22 Durán, O., Claudin, P. & Andreotti, B. On aeolian transport: Grain-scale interactions, dynamical mechanisms and scaling laws. *Aeolian. Res.* **3**, 243-270 (2011).

23 Martin, R. L. & Kok, J. F. Wind-invariant saltation heights imply linear scaling of aeolian saltation flux with shear stress. *Sci. Adv.* **3**, e1602569 (2017).

24 Jasper, F. K., Eric, J.-R.-P., Timothy, I. M. & Diana-Bou, K. The physics of wind-blown sand and dust. *Rep. Prog. Phys.* **75**, 106901 (2012).

25 Fryberger, S. G. Techniques for the evaluation of surface wind data in terms of eolian sand drift. United States Geological Survey, Open-File Report 78-405 (1978).

26 Fryberger, S. G. *Dune forms and wind regimes.* In *A study of global sand seas* [McKee, E. D. (ed)]. United States Geological Survey, 137-169 (1979).

27 Baas, A. C. W. & Delobel, L. A. Desert dunes transformed by end-of-century changes in wind climate. *Nat. Clim. Chang.* **12**, 999–1006 (2022).

28 Michel, S. et al. Comparing dune migration measured from remote sensing with sand flux prediction based on weather data and model, a test case in Qatar. *Earth Planet. Sci. Lett.* **497**, 12-21 (2018).

29 Yizhaq, H., Xu, Z. & Ashkenazy, Y. The effect of wind speed averaging time on the calculation of sand drift potential: New scaling laws. *Earth Planet. Sci. Lett.* **544**, 116373 (2020).

30 Hersbach, H. et al. The ERA5 global reanalysis. *Q. J. Roy. Meteor. Soc.* **146**, 1999-2049 (2020).

31 Muñoz-Sabater, J. et al. ERA5-Land: a state-of-the-art global reanalysis dataset for land applications. *Earth Syst. Sci. Data* **13**, 4349-4383 (2021).

32 Wu, H. J., Lu, H. Y., Wang, J. J., Chen, Y. & Cui, M. C. A new estimate of global desert area and quantity of dust emission (in Chinese). *Chin. Sci. Bull.* **67**, 860-871 (2022).

33 Vermeesch, P. & Drake, N. Remotely sensed dune celerity and sand flux measurements of the world's fastest barchans (Bodélé, Chad). *Geophys. Res. Lett.* **35**, L24404 (2008).

34 Shao, Y. Physics and modelling of wind erosion (2nd ed.). (Springer Netherlands, 2008).

35 Kok, J. F. et al. An improved dust emission model – Part 1: Model description and comparison against measurements. *Atmos. Chem. Phys.* **14**, 13023-13041 (2014).

36 Dunnett, S., Sorichetta, A., Taylor, G. & Eigenbrod, F. Harmonised global datasets of wind and solar farm locations and power. *Sci. Data* **7**, 130 (2020).

37 Kocurek, G. & Havholm, K. G. *Eolian sequence stratigraphy - a conceptual framework*. In *Siliciclastic sequence stratigraphy: recent developments and applications* [Weimer, P. and Posamentier, H. (eds.)], 393-409 (1993).

38 Lancaster, N. *Sand seas and dune fields*. In: Shroder, J. (Editor in Chief), Lancaster, N., Sherman, D.J., Baas, A.C.W. (Eds.), *Treatise on Geomorphology*. Academic Press, San Diego, CA, vol. 11, *Aeolian Geomorphology*, pp. 219–245 (2013).

39 Gadal, C. et al., Local wind regime induced by giant linear dunes: comparison of ERA5-Land Reanalysis with surface measurements. *Bound-Lay. Meteorol.* 185, 309-332 (2022).

40 Li, G. et al., More extreme precipitation in Chinese deserts from 1960 to 2018. *Earth Space Sci.* **6**, 1196-1204 (2019).

41 United Nations General Assembly. *Transforming our world: The 2030 agenda for sustainable development*. (December 2015).

42 Rogelj, J. et al. Zero emission targets as long-term global goals for climate protection. *Environ. Res. Lett.* **10**, 105007 (2015).

43 Liu, H. et al. Annual dynamics of global land cover and its long-term changes from 1982 to 2015, *Earth Syst. Sci. Data* **12**, 1217–1243 (2020).

44 Gunn, A. et al., Macroscopic flow disequilibrium over aeolian dune fields. *Geophys. Res. Lett.* **47**, e2020GL088773 (2020).

45 Bagnold, R. A. The physics of blown sand and desert dunes. (Methuen, New York, 1941).

46 Lettau, K. & Lettau, H. H.: *Experimental and micro-meteorological field studies of dune migration (IES Report, 101, 110–147)*, in *Exploring the world's driest climate* [Lettau, H. H. and Lettau, K. (eds.)], University of Wisconsin-Madison, Institute for Environmental Studies, Madison, WI (1978).

47 Namikas, S. L. Field measurement and numerical modelling of aeolian mass flux distributions on a sandy beach. *Sedimentology* **50**, 303-326 (2003).

48 Yao, Z., Chen, G., Han, Z. & Shao, G. Mechanical properties of aeolian sandy soil in central Taklimakan Desert. *J. Des. Res.* **21**, 28-33 (2001).

49 Yuan, Y. & Wang, X. Experimental research on compaction characteristics of aeolian sand. *Chinese J. Geotech. Eng.* **29**, 360-365 (2007).

50 Yang, X., Wang, Y., Gui, D. & Jia, L. Physical and mechanical characters of sands in Gurbantonggut Desert. *J. Des. Res.* **25**, 563-569 (2005).

51 Yang, Z., Hou, Y., Kong, H. & Li, L. Compaction property of eolian sand and its deformation behavior under cyclic loading. *China J. Highway Transport* **15**, 8-10 (2002).

52 Pang, Y. *The aeolian environment and dynamic characteristics of the dunes at the Crescent Moon Spring scenic spot of Dunhuang, China*. in *Northwest*

Institute of Eco-Environment and Resources, CAS (University of Chinese Academy of Sciences, Lanzhou), p 97 (2014).
53 Wu, Z. Geomorphology of wind-drift sands and their controlled engineering (Science Press, Beijing, China, 2003).
54 Xu, L. et al. Variations of soil physical properties in desertification revsersion process at south edge of Tengger Desert. *J. Des. Res.* **28**, 690-695 (2008).
55 Yang, Y. & Cheng, R. Feasibility study on engineering property of aeolian sand and application as dam backfill material. *Yellow River* **36**, 95-97 (2014).
56 Hai, L., Wang, X., Hu, E. & Zhang, L. Soil physical and chemical properties in several sandy lands in Inner Mongolia. *J. Inner Mongolia For. Sci. Technol.* **36**, 6-10 (2010).
57 Jiao, L. & Wang W. Experimental research on compaction characteristics of aeolian sand subgrade. *J. Water Resour. Archit. Eng.* **10**, 22-26 (2012).
58 Yang, Y., Liu, L., Cao, H. & Jia, Z. Change of soil physical properties from desert area to loess area in China. *J. Des. Res.* **33**, 146-152 (2013).
59 Fan, N. & Wang, S. Effects of vegetation restoration on physical and chemical characteristics of the soil in Hunshandake Sand. *J. Anhui Agr. Sci.* **42**, 10736-10737 (2014).
60 Mueller, R., Schulzweida, U., Kornbuleh, L. & Modali, K. Climate Data Operators (CDO) software, https://code.mpimet.mpg.de/projects/cdo (2013).
61 Bergin, M. H., Ghoroi, C., Dixit, D., Schauer, J. J. & Shindell, D. T. Large reductions in solar energy production due to dust and particulate air pollution. *Environ. Sci. Tech. Lett.* **4**, 339-344 (2017).
62 OpenStreetMap contributors. Elements. OpenStreetMap Wiki, https://wiki.openstreetmap.org/wiki/Elements (2019).

ACKNOWLEDGMENTS

We thank Huayu Lu and Huijuan Wu for providing the data of desertified lands and sandy lands with 500 m resolution. This research was supported by the Strategic Priority Research Program of Chinese Academy of Sciences under grant No. XDA20100104 and the National Natural Science Foundation of China (grant No. 41901377). F.C.L. was supported by the Swedish Research Council (Vetenskapsrådet, grant no. 2018-01272) and conducted the work with this article as a Pro Futura Scientia XIII Fellow funded by the Swedish Collegium for Advanced Study through Riksbankens Jubileumsfond.

AUTHOR CONTRIBUTIONS

G.L., L.T., B.Y. and X.L. designed research; G.L. and B.Y. performed research and analyzed data; G.L., L.T., T.C., Y.L., H.D., H.Z., Y.Z., C.H., R.J. and X.L. contributed analytic tools; G.L., L.T., B.Y., G.F., F.C.L., N.H., W.T. and X.L. wrote the paper.

COMPETING INTERESTS

The authors declare no competing interest.

ADDITIONAL INFORMATION

Supplementary Fig. S1.
Supplementary Table S1.

FIGURE LEGENDS

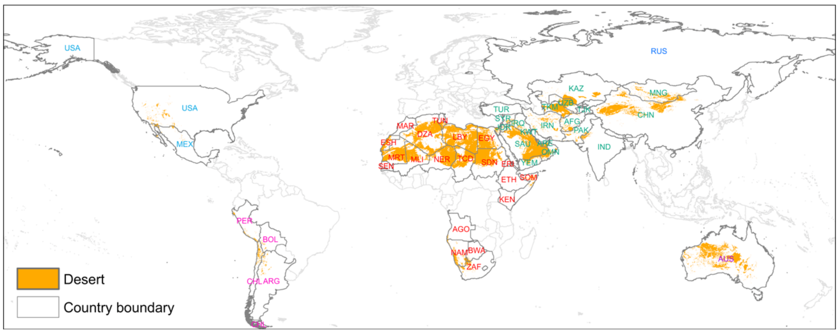

Fig. 1 Spatial distribution of global deserts.

Deserts are resampled to a resolution of 0.1°×0.1°, matching the spatial resolution of the ERA5-Land hourly wind data. The colored abbreviations are the three letter ISO 3166-1 alpha-3 GADM country codes. The countries in Asia are colored by the malachite green, the countries in Africa the mars red, the countries in South America the ginger pink, the countries in North America the moorea blue, the countries in Europe the cretan blue, and the countries in Australasia the anemone violet. The boundaries of the country with desert data are colored by 50% gray, and the rest are colored by 10% gray.

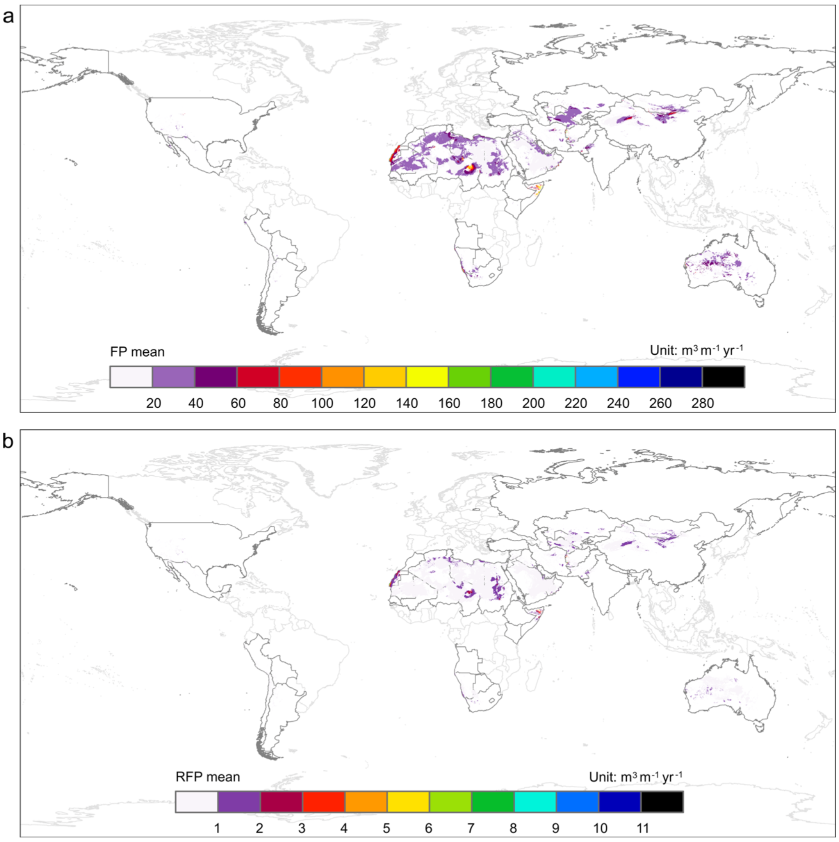

Fig. 2 The (a) FP and (b) RFP means of global deserts for the period 1950–2022.

The equidistant spacings of the FP and RFP means are set to 20 m^3 m^{-1} yr^{-1} and 1 m^3 m^{-1} yr^{-1}, respectively.

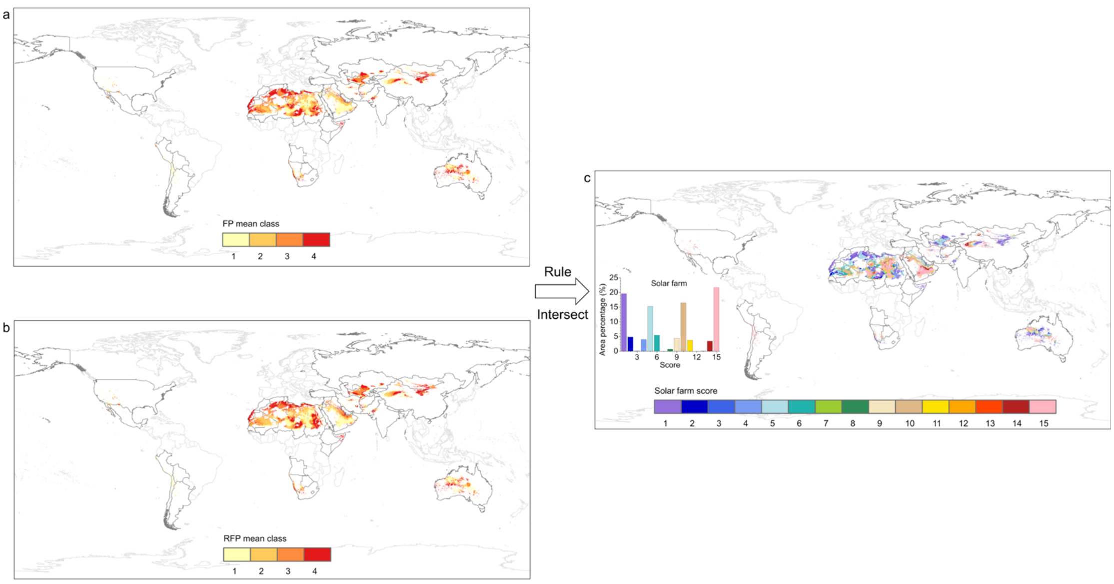

Fig. 3 The scoring scheme and result for solar farms based on changes in sand flux.

First intersect the (**a**) FP and (**b**) RFP mean classes, then remove non-observed permutations, and finally apply the simple rule to assign the corresponding scores for solar farms (**c**). The left insets show the percentage distribution of geodesic area for solar farm scores.

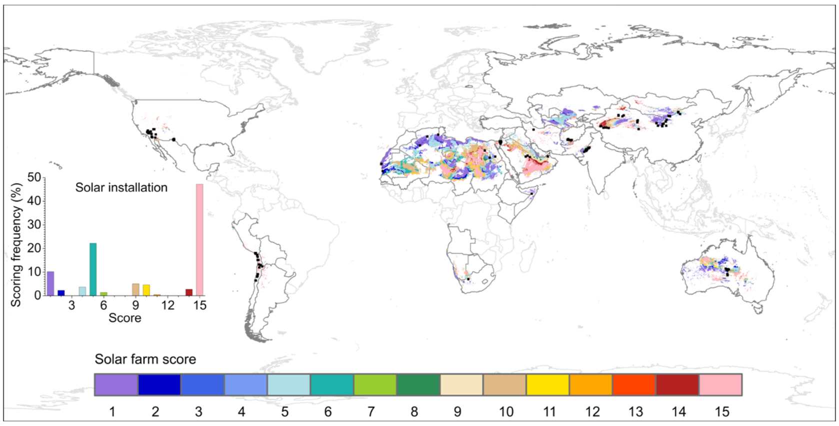

Fig. 4 Validation of solar farm scores in deserts.

The black solid squares represent the locations of the 216 solar installations in deserts. The inset presents the scoring frequencies extracted by the existing solar installations in deserts.

TABLE

Table 1. Solar farm scores across global deserts.

The FP and RFP means are divided into 4 classes separately using quartile classification, respectively. High (low) score indicates a strong (weak) suitability. For building solar farms, we should consider other factors besides the scores. The area percentage refers to the geodesic area of the assigned score accounting for the geodesic area of all scores (global deserts), and the scoring frequency refers to the installation number of solar farms located in the assigned score accounting for that of all solar farms in deserts (216).

FP mean	RFP mean	Score	Grid point number	Geodesic area (10^3km^2)	Area percentage (%)	Scoring frequency (%)
4	4	1	19846	2106.19	19.63	10.19
4	3	2	4664	522.51	4.87	2.31
4	2	3	86	10.06	0.09	
3	4	4	4071	432.11	4.03	3.70
3	3	5	15369	1644.77	15.33	22.22
3	2	6	5139	586.35	5.46	1.39
3	1	7	15	1.78	0.02	
2	4	8	677	75.84	0.71	
2	3	9	4505	476.51	4.44	5.09
2	2	10	15901	1766.24	16.46	4.63
2	1	11	3512	401.77	3.74	0.46
1	4	12	1	0.10	0.00	
1	3	13	57	6.15	0.06	
1	2	14	3469	367.40	3.42	2.78
1	1	15	21068	2333.28	21.74	47.22

Supplementary Information

Site selection of desert solar farms based on heterogeneous sand flux

Guoshuai Li et al.

Corresponding email: Xin Li, xinli@itpcas.ac.cn

Supplementary Figure

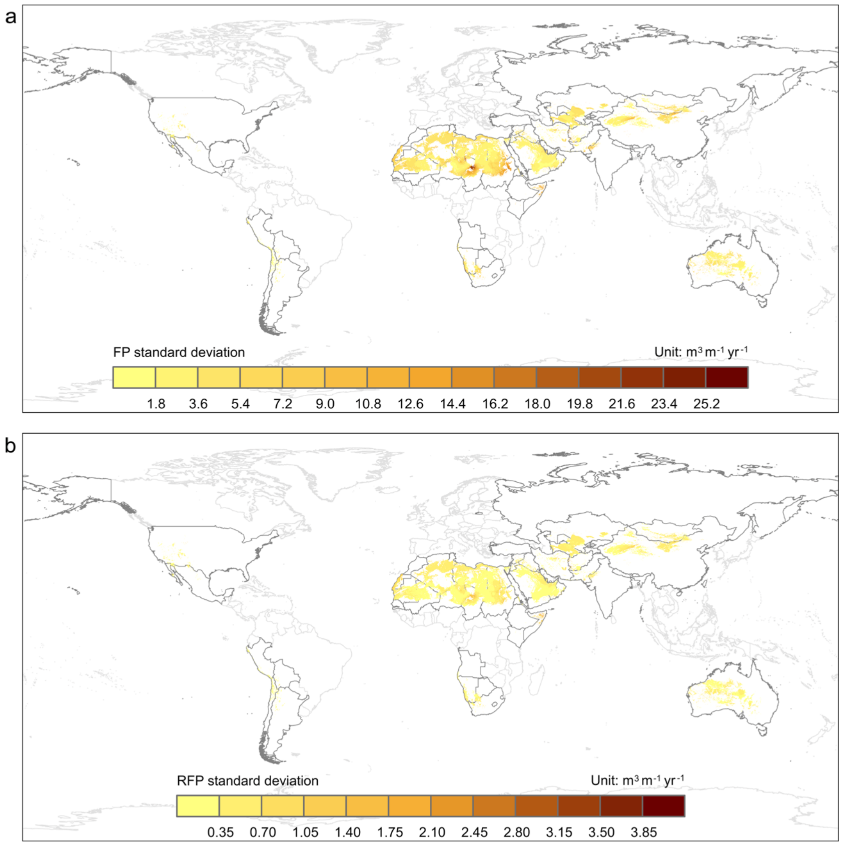

Fig. S1 Spatial distributions of the standard deviations of the (a) FP and (b) RFP for the period 1950–2022.

(a) and (b) adopt the interval size of 1.8 m^3 m^{-1} yr^{-1} and 0.35 m^3 m^{-1} yr^{-1}, respectively. The boundaries of the country with desert data are colored by 50% gray, and the rest are colored by 10% gray.

Supplementary Table

Table S1. Bulk densities (g cm^{-3}) in other studies.

The TakD, GTD, QaiD, KumD, BJD, TenD, HobD, MUS, HunS, HulS and HorS are the abbreviations of the Taklamakan Desert, Gurban Tunggut Desert, Qaidam Desert, Kumtag Desert, Badain Jaran Desert, Tengger Desert, Hobq Desert, Mu Us Sandy land, Hunshandake Sandy land, Hunlunbuir Sandy land and Horqin Sandy land in China, respectively[40].

Name	Bulk density	Notes	Source
TakD	1.45, 1.45, 1.43, 1.43, 1.59, 1.59, 1.7, 1.7, 1.54, 1.54, 1.58, 1.58	Tazhong, Xinjiang	Yao et al., 2001[48]
TakD	1.385	Hinterland TakD	Yuan & Wang, 2007[49]
TakD	1.715	Eastern TakD	Yuan & Wang, 2007[49]
GTD	1.57, 1.56, 1.59, 1.59, 1.61, 1.61, 1.59, 1.61, 1.6, 1.61, 1.57, 1.6, 1.59, 1.62, 1.58, 1.61, 1.61, 1.62, 1.59, 1.6, 1.58, 1.61, 1.61, 1.6, 1.58, 1.6, 1.61, 1.62, 1.57, 1.6, 1.59, 1.62, 1.6, 1.62, 1.6, 1.62, 1.56, 1.6, 1.59, 1.61, 1.55, 1.62, 1.6, 1.59, 1.59, 1.59, 1.57, 1.61, 1.6, 1.61, 1.59, 1.62, 1.57, 1.6, 1.57, 1.6, 1.59, 1.6, 1.59, 1.59, 1.59, 1.56, 1.61		Yang, et al., 2005[50]
GTD	1.69	Southern GTD	Yuan & Wang, 2007[49]
QaiD	1.76	Geermu, Qinghai	Yang et al., 2002[51]
KumD	1.58	Dashagou, Gansu	Pang, 2014[52]
BJD	1.6	Linze, Gansu	Wu, 2003[53]
TenD	1.5	Minqing, Gansu	Wu, 2003[53]
TenD	1.63	Zhongwei, Ningxia	Wu, 2003[53]
TenD	1.56	Southern TenD	Xu et al., 2008[54]
UBD	1.56	Southeastern UBD	Yuan & Wang, 2007[49]
UBD	1.63		Yang & Cheng, 2014[55]
HobD	1.49, 1.44, 1.43		Hai et al., 2010[56]
MUS	1.2	Hinterland MUS	Yuan & Wang, 2007[49]
MUS	1.56	Border crossing between MUS and Yulin, Shanxi	Yuan & Wang, 2007[49]
MUS	1.45	Ranging between 1.4 and 1.5	Jiao & Wang, 2012[57]

MUS	1.53		Yang, et al., 2013[58]
HunS	1.73, 1.72, 1.62		Fan & Wang, 2014[59]
HorS	1.69	Kezuohouqi, Neimenggu	Wu, 2003[53]
HorS	1.52, 1.49, 1.48, 1.49		Hai et al., 2010[56]